Sulfation of PdO(101) Methane Oxidation Catalyst: Mechanism Revealed by First Principles Calculations

Journal:	*Catalysis Science & Technology*
Manuscript ID	CY-ART-10-2018-002096.R1
Article Type:	Paper
Date Submitted by the Author:	15-Nov-2018
Complete List of Authors:	Arevalo, Ryan; National Institute of Technology, Akashi College, ; employer Aspera, Susan; National Institute of Technology, Akashi College, Nakanishi, Hiroshi; National Institute of Technology, Akashi College; Osaka University, Department of Applied Physics

Catalysis Science & Technology

ARTICLE

Sulfation of PdO(101) Methane Oxidation Catalyst: Mechanism Revealed by First Principles Calculations

Received 00th January 20xx,
Accepted 00th January 20xx

DOI: 10.1039/x0xx00000x

www.rsc.org/

Ryan Lacdao Arevalo[a], Susan Meñez Aspera[a], Hiroshi Nakanishi[a,b,c,*]

PdO efficiently catalyzes the oxidation of methane but suffers tremendously from sulfur poisoning that lowers its catalytic activity. In this work, first principles calculations were performed to reveal the mechanism of PdO(101) sulfation and how the active sites for methane activation are altered upon the formation of SO_y (y = 2 to 4) species on the surface. Results suggest that at typical experiment conditions with high O_2/SO_2 gas ratio, the formation of SO_4-decorated PdO(101) is favored and contributes significantly to the poisoning of PdO(101) as it blocks the coordinatively unsaturated Pd atoms that were identified to play a crucial role in the activation of methane. At low temperature regime, SO_2 oxidation forming SO_3 and SO_4 species is highly exothermic via the Eley-Rideal and Langmuir-Hinshelwood mechanisms but is limited by the high activation barrier for O_2 dissociation. On the other hand, the Mars-van Krevelen mechanism has low exothermicity but provides facile elementary steps. From these results, insights into the design of PdO-based sulfur poisoning-resistant methane oxidation catalysts were drawn.

1. Introduction

Catalyst poisoning is a long-standing problem in the heterogeneous catalysis of a wide range of reactions such as oxidation, hydrogenation, reforming of hydrocarbons, and ammonia production.[1] It often involves compounds that strongly bond with the active sites of catalysts, thereby decreasing the catalytic activity and/or selectivity. Over the past years, many research works were conducted to understand the mechanism of various catalyst poisoning reactions to provide insights into the design of poison-resistant catalysts and optimization of processes to prevent or slow catalyst deactivation.[1-8]

Sulfur poisoning is a major concern in the catalytic oxidation of methane.[9-11] It is due mainly to sulfur contained in the natural gas itself (as odorizer) or from engine lubricating oil in combustion systems.[9] Over the past decades, experiments were conducted to understand the mechanism of this reaction on various supported and unsupported catalysts such as mono and bimetallic Pt and Pd on Al_2O_3, CeO_2, ZrO_2, SiO_2, Y_2O_3, and La_2O_3, using techniques such as X-ray photoelectron spectroscopy (XPS), Fourier transform infrared spectrometer (FT-IR), X-ray diffraction (XRD), scanning transmission electron microscopy (STEM), operando X-ray absorption near edge spectroscopy (XANES), among others.[9,11-19] These studies sought to identify the effects of support,[12,16-17] catalyst size and composition,[11,16,18,20] various experimental conditions,[14-15] and catalyst regeneration.[17-18,21]

Pd-based catalysts have excellent activity for methane oxidation under net oxidizing conditions but suffer tremendously from sulfur poisoning.[12,15-19] A general consensus suggests that Pd exists in the form of an oxide when methane oxidation proceeds under oxygen rich conditions and temperatures below 950 K.[22-23] In situ XRD and XPS measurements showed that PdO(101) develops preferentially during the oxidation of Pd(100).[24-26] Its formation coincides with the increased rates of methane oxidation,[26] suggesting PdO formation to be responsible for the exceptional activity of Pd-catalysts for the catalytic combustion of methane.[27-28] Because of this, significant experimental efforts were directed toward understanding the mechanism of sulfur poisoning on PdO methane oxidation catalysts.

Experiments found the formation of sulfites and sulfates on Pd catalysts, which are believed to poison or deactivate the active sites for methane oxidation.[12,15-19] Lambert et al. confirmed through an XPS of unsupported PdO treated with SO_2 or SO_3 the formation of a surface skin of SO_4^{2-} and the increase in the degree of Pd oxidation state as evidenced by the increase in the Pd $3d_{5/2}$ electron binding energy.[16] From these results, it was inferred that the deactivation of PdO by SO_2 may be due to both the decrease in the chemisorption of methane as surface sulfate layer is formed, and the decrease in the availability of oxygen from PdO due to an increase in the Pd oxidation state. In more recent XPS, FT-IR, and XRD experiments on unsupported PdO, Mowery et al. similarly found a rapid, permanent, and compete deactivation of PdO due to the sulfation of the surface layer. Furthermore, XRD of deactivated catalysts indicates the presence of Pd^0, which was proposed to form through the oxidation of SO_2 to SO_3.[15] Recently, a

[a] National Institute of Technology, Akashi College, 679-3 Nishioka, Uozumi, Akashi, Hyogo 674-8501, Japan
[b] Graduate School of Engineering, Osaka University, 2-1 Yamadaoka, Suita, Osaka 565-0871, Japan
[c] Institute of Industrial Science, The University of Tokyo, Meguro, Tokyo 153-8505, Japan
*Corresponding Author: nakanishi@akashi.ac.jp

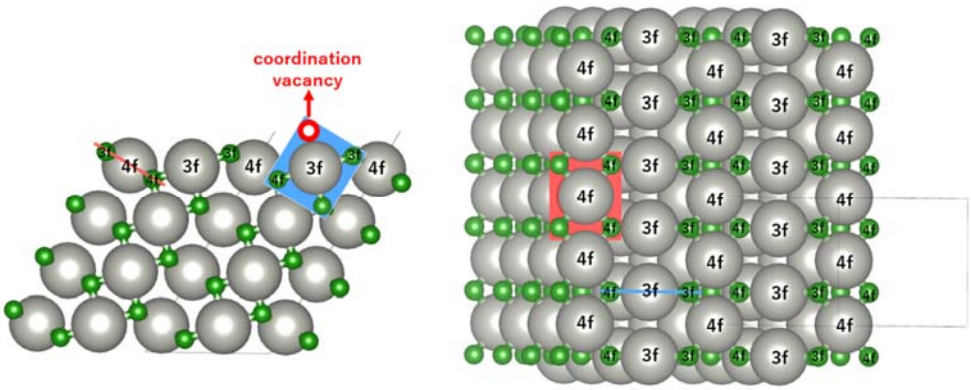

Figure 1: The side (left) and top (right) views of the slab model for PdO(101) surface. Gray and green atoms represent Pd and O, respectively. Pd and O atoms on the surface are marked as 3f or 4f, indicating a 3-fold or 4-fold coordination. The coordination plane for Pd_{3f} and Pd_{4f} atoms are shown by the blue and red planes, respectively.

theoretical study showed that the formation of $PdSO_4$ and adsorption of SO_3 and oxygen species are highly favored on clean and oxidized Pd surfaces at typical temperature and pressure conditions.[10]

As the literature is scarce on theoretical studies of the sulfation of PdO as methane oxidation catalyst, a molecular understanding on how SO_4 forms on the surface of PdO remains speculative. In particular, it is imperative to identify the mechanistic paths toward SO_4 formation on PdO(101) surface and describe how the active sites for methane activation are altered by the adsorption and subsequent oxidation of SO_2. In this contribution, first principles calculations based on density functional theory with van der Waals correction was used to reveal the mechanism of PdO(101) sulfation in relation to the activation of methane. In the first part, the electronic structure of PdO(101) is presented to predict the reactive sites on the surface and identify the relevant components of the Pd d band in the bonding of molecules on the surface. In the second part, methane activation on PdO(101) is revisited to clarify and expound the literature-proposed mechanism of C–H bond activation by the coordinatively unsaturated Pd atom. In the last part, a mechanistic study of SO_2 oxidation is presented and discussed in relation to methane activation and insights to catalysts design.

2. Results and Discussion

A monoxide compound PdO (space group 131, *$P4_2/mmc$*) is the only known stable oxide of Pd.[10] The calculated lattice constants are a = 3.06 Å and c/a = 1.77, in excellent agreement with experiments (a = 3.04 Å and c/a = 1.75).[29-30] Figure 1 shows the side and top views of the PdO(101) surface, which was modeled using a slab with four Pd layers in a 1×2 supercell (16 Pd and 16 O atoms) with ca. 12 Å of vacuum space. Pd atoms on the surface are marked as either 3f or 4f to denote the 3-fold and 4-fold coordinated Pd atoms, which are respectively referred to in this paper as Pd_{3f} and Pd_{4f} atoms. Pd forms a square planar coordination with O atoms as shown by the red and blue planes in Fig. 1. Pd_{3f} is coordinatively unsaturated (cus) with a coordination vacancy on top of the Pd_{3f} atom. O atoms on the surface are also marked as either 3f or 4f based on their coordination with Pd atoms, which are also referred to in this paper as O_{3f} and O_{4f} respectively. O_{3f} atoms protrude out of the surface while O_{4f} atoms bond with the subsurface atoms. The coordination plane of the unsaturated Pd_{3f} atom is perpendicular to the surface, while that of the Pd_{4f} atom is tilted with respect to the (101) surface.

2.1. Electronic Structure of PdO(101)

In PdO, the Pd atoms are oxidized while O atoms reduced. As shown by the Bader charges reported in Table 1, the Pd_{4f} atoms have lost more electrons than Pd_{3f} because more O atoms are coordinated to the Pd_{4f} atom. Correspondingly, more electrons are gained by O_{4f} than O_{3f} because of the difference in their coordination with Pd atoms. These observations correspond to the change in the electronic structure of a non-oxide Pd atom shown in Fig. 2a, as it forms an oxide. In this figure, the local density of states projected on the d band of Pd atom at the step edge of Pd(211) surface (representing a pure Pd metal) and the Pd_{3f} and Pd_{4f} atoms of PdO(10) surface are shown by blue, black, and red curves, respectively. Correspondingly, the sp states of O_{3f} and O_{4f} atoms are shown in Fig. 2b. With respect to the d band of a non-oxide Pd(211), there is an emergence of unoccupied states above the Fermi level in the d band of both Pd_{3f} and Pd_{4f} atoms of PdO(101). A

Table 1: Bader charges (in unit of electron) of the surface atoms of PdO(101)

Pd		O	
3f	4f	3f	4f
+0.76	+0.98	–0.85	–0.96

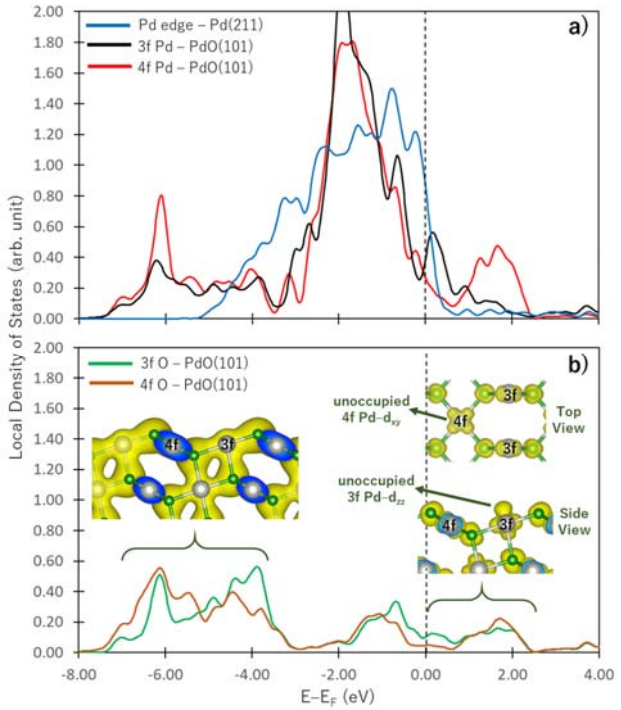

Figure 2: Local density of states projected on the d band of Pd (part a) and sp states of O (part b). Blue, black, and red curves in part a are respectively: the d bands of Pd atom at the step edge of Pd(211), and Pd_{3f} and Pd_{4f} atoms of PdO(101). The inset figures in part b show the partial charge density plots projected at energy ranges bound by the bracket at an isosurface value of 0.0144505 e/a_0^3. The blue region in the inset figures show the "slicing plane" where the charge density plot was terminated.

broader unoccupied state is seen for Pd_{4f}, corroborating its noted greater electron loss in the Bader charge analysis. At the energy range below –4.00 eV, new states are formed in the d band of Pd_{3f} and Pd_{4f} atoms with respect to the d band of pure Pd atom. These states hybridize with the sp states of O shown in Fig. 2b, indicating the Pd-d and O-sp bonding states. The partial charge density plot projected at this energy range (left inset figure in Fig. 2b) shows the covalent bond between Pd and O atoms.

Interestingly, the partial charge density plots projected at the energy range above the Fermi level (right inset in Fig. 2b) show the different characteristics of the unoccupied states of Pd_{3f} and Pd_{4f} atoms. For Pd_{3f} atoms, the unoccupied state has a d_{zz} character, which stems from the presence of O atom directly below the Pd_{3f} atom. This unoccupied d_{zz} state of Pd_{3f} hints its higher affinity toward electron donation from the σ-type molecular orbital of adsorbates. Assigning the Pd_{3f} coordination plane as xz plane, the corresponding occupied states of the Pd_{3f} d band has d_{yz} character. On the other hand, for the case of Pd_{4f}, similar analysis indicates that the unoccupied states of its d band have d_{xy} characteristics. Because the Pd_{4f} atoms are rectangularly coordinated to 4 O atoms on the xy plane, its d_{xy} orbital is depopulated. Correspondingly, the d_{zz} orbital of Pd_{4f} is occupied, which is expected to yield to a repulsive interaction toward the σ-type molecular orbital of adsorbates. As the Pd atoms in PdO are oxidized, they have higher affinities for electron donation from adsorbates and reduced tendencies for backdonation. By its spatial distribution, the Pd_{3f}–d_{zz} can facilitate electron donation, resulting in the greater reactivity of Pd_{3f} compared to Pd_{4f}.

2.2 Revisiting Methane Activation on PdO(101)

Methane activation and oxidation on PdO(101) were studied in recent DFT calculations.[30-32] Though methane

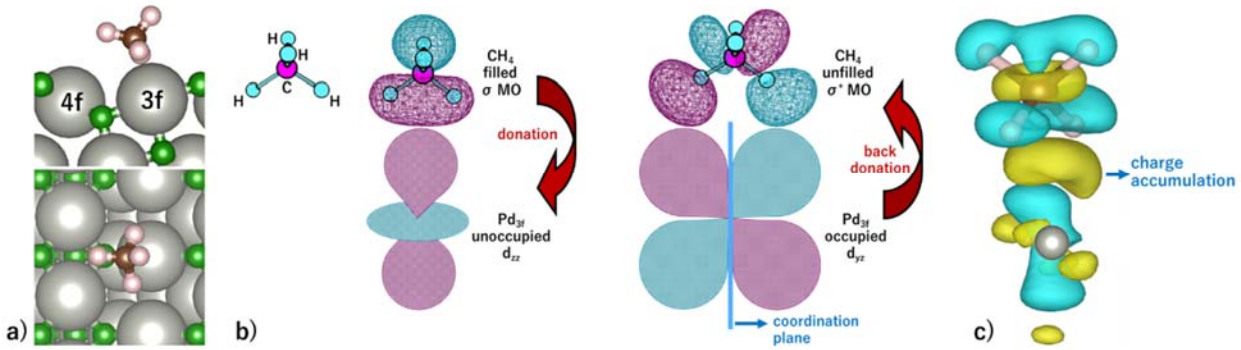

Figure 3: a) Optimal adsorption configuration of CH_4 on PdO(101) surface. b) Mechanism of electron donation and back-donation between CH_4 and the coordinatively unsaturated Pd atom. Lobes of the same color denote the same phase of the wavefunction. The molecular orbitals of the gas phase CH_4 were calculated using the GAUSSIAN code[55] with B3LYP functional with 6-31G(d,p) basis sets. c) Charge density difference upon the adsorption of CH_4 on the PdO(101), computed using $\Delta\rho = \rho_{CH_4^*} - (\rho_{CH_4} + \rho_*)$, where each term to the right denotes the charge density of the CH_4 + slab complex, and the summed charge densities of isolated CH_4 gas and slab. Yellow and cyan colors represent charge accumulation and depletion, respectively, rendered using VESTA.[55]

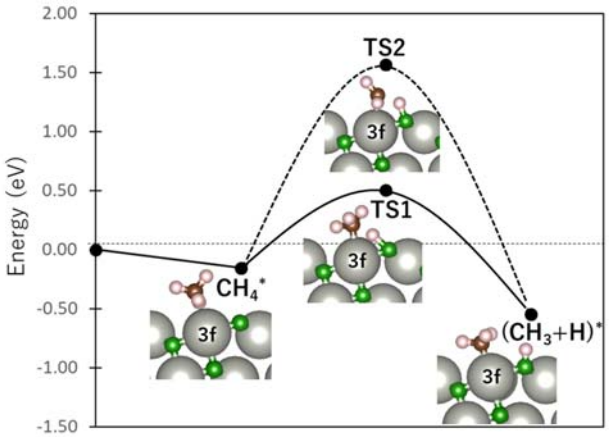

Figure 4: Energy profile of CH_4 dissociation. TS1 and TS2 denote the transition states for the cleaving of the Pd-coordinated ("activated") and non-interacting C–H bonds, respectively.

oxidation pathway is a subject of an ongoing debate, there is a general consensus that the initial C–H bond activation of methane is the main limiting step.[31-32] Weaver et al. proposed that methane forms dative bonds with the coordinately unsaturated Pd atoms, resulting in a σ complex whose bonding involves electron donation and back-donation.[31] However, considering that charge density difference only accounts for the initial and final states of the system, drawing a model for this donor-acceptor interaction remains to be a challenge from their analysis of the charge density difference upon CH_4 adsorption on PdO(101). Bossche and Gronbeck used first principles kinetic modeling of methane oxidation over PdO(101) and revealed that oxidation steps subsequent to the initial methane activation take place through Mars-van Krevelen mechanisms.[32] Nevertheless, as earlier mentioned that experiments predicted PdO deactivation by SO_2 to originate from the decrease of CH_4 chemisorption on the surface, a confirmation of the active site for CH_4 activation is an important step in understanding the mechanism of sulfur poisoning on a PdO(101) methane oxidation catalyst.

Figure 3a shows the optimal adsorption configuration of CH_4 on PdO(101). The two C–H bonds are coordinated with the Pd_{3f} atom while the other two C–H bonds point away from the surface. This confirms the earlier predicted reactivity of the Pd_{3f} from the analysis of its electronic structure. Considering the identified unoccupied d_{zz} and occupied d_{yz} states of Pd_{3f} atom earlier mentioned, the mechanism of electron donation and back-donation between CH_4 and Pd_{3f} can be drawn. The highest occupied molecular orbital of CH_4 is a three fold degenerate σ-type molecular orbital ($1t_2$) as shown in Fig. 3b. This filled molecular orbital can donate electrons to the unoccupied d_{zz} state of Pd_{3f}. The occupied Pd_{3f}–d_{yz} orbital can facilitate the back-donation to an unfilled σ^* molecular orbital of CH_4. Considering the phase and spatial configuration of the unfilled CH_4 molecular orbitals, the $2t_2$ molecular orbital can facilitate the back-donation from the occupied Pd_{3f}–d_{yz} orbital as shown in Fig. 3b. This back-donation results in the weakening of the two C–H bonds coordinated to the Pd_{3f} atom. We found that these "activated" C–H bonds are elongated by 21 mÅ with respect to the gas-phase C–H bonds of methane. The charge density difference in Fig. 3c shows an accumulation of charge between CH_4 and Pd_{3f}, which Weaver et al. attributed to a dative covalent bond.[31]

Figure 4 shows an energy profile for the dissociation of CH_4 into CH_3 + H. At the final state, CH_3 bonds with the Pd_{3f} atom while the O_{3f} atom acts as H-acceptor, forming a CH_3-Pd_{3f} and H-O_{3f} moieties. Transition states were calculated using the Dimer method, with the initial direction along the dimer generated based on initial and final states.[33-36] The activated (TS1) and non-interacting (TS2) C–H bonds required activation barriers of 0.66 eV and 1.72 eV, respectively. For comparison, the calculated values of Weaver et al. using DFT without van der Waals correction are 0.67 eV and 1.73 eV for TS1 and TS2 activation barriers, respectively, while that of Chin et al. is 0.64 eV for TS1 activation barrier using ultrasoft pseudopotentials.[37-38] This confirms the weakening of the Pd_{3f} coordinated C–H bonds through back donation to the $CH_4 - \sigma^*$ molecular orbital. The C–H bond activation of methane on IrO_2(110) was also attributed by Wang et al. on σ–d interaction of CH_4 and coordinatively unsaturated Ir atom.[39] Following the initial activation of methane, DFT-based microkinetic modeling and kinetic isotope studies found that the subsequent reactions with O follow a Mars-van Krevelen mechanism, where O atoms from the substrates are used to produce carbon dioxide and water.[32,40]

2.3 SO_2 Oxidation on PdO(101)

Results from the previous section have shown that the Pd_{3f} and O_{3f} atoms on PdO(101) play important roles in the activation of methane. It can be argued that blocking these active sites with other adsorbates can decrease the activity of the catalyst for methane activation. As shown in Fig. 5a, the adsorption of SO_y (y = 2 to 4) type of molecules involve both the Pd_{3f} and Pd_{4f} atoms, suggesting a possible poisoning of the Pd_{3f} site. SO_2 forms two O–Pd_{3f} and one S–Pd_{4f} bonds on the surface, with adsorption energy of –1.74 eV. This value of adsorption energy is more than ten times greater than that of CH_4 (–0.16 eV). This explains why sulfur poisoning is still prominent despite its very low concentration (1 ppm or less) in typical experiment conditions.[9] It can be noted that another DFT calculation showed that water molecule also blocks the Pd sites on PdO(101) with a sizeable adsorption energy (ca. –1.3 eV), which explains the experimentally observed water inhibition of methane adsorption on the surface.[32] SO_3 and SO_4 form similar bonding characteristics on the surface, i.e., forming bonds with two Pd_{3f} and one Pd_{4f} atoms. The calculated Bader charges of S in SO_2, SO_3, and SO_4 adsorbed on the surface are +3.2e, +4.9 e, and +6.0e, respectively, indicating the different oxidation states of S on these systems. Correspondingly, O gained electrons because its high electronegativity. The stabilities of adsorbed species SO_y^* (y = 2, 3, 4) and O_2^* were compared by calculating

its free energy change with respect to gas-phase O_2, SO_2, and the clean PdO(101) surface. That is:

$$\Delta G_{SO_y^*} = G_{SO_y^*} - G_* - \mu_{SO_2} - \left(\frac{y-2}{2}\right)\mu_{O_2}$$

$$\Delta G_{O_2^*} = G_{O_2^*} - G_* - \mu_{O_2}$$

The asterisk "*" denotes surface-bound species, while the molecules with no asterisk denote the gas-phase species. The chemical potentials μ of gas-phase species SO_2 and O_2were computed by adding the DFT calculated total energy, zero point vibrational energy, and the temperature and pressure dependent parts of the chemical potential:

$$\mu_{SO_2} = E_{SO_2}^{DFT} + E_{SO_2}^{ZPVE} + \Delta\mu_{SO_2}(T,p)$$

$$\mu_{O_2} = E_{O_2}^{DFT} + E_{O_2}^{ZPVE} + \Delta\mu_{O_2}(T,p)$$

The temperature dependence of free energies for the condensed phases (i.e., SO_y^*, O_2^* and slab) were shown to have no significant impact in constructing phase diagrams and is thus ignored in this calculation.[10]

Figure 5b shows the phase diagram with clean PdO(101) surface (denoted by asterisk to indicate an "empty" site), and PdO(101) surface with adsorbed O_2, SO_2, SO_3, and SO_4 in the given range of SO_2 and O_2 chemical potentials, which are translated into a pressure range for T = 400 °C. Essentially, the figure shows the most stable (i.e., the one with lowest free energy) $S_xO_y^*$ species for a given chemical potential of SO_2 and O_2. At typical experiment conditions[9] where the chemical potential of O_2 of ca. –1.7 eV, the phase diagram shows the preference towards the bare PdO surface for SO_2 chemical potential lower than ca. –2.5 eV. For the same O_2 chemical potential, increasing the SO_2 chemical potential to values typical in experiments (ca. –2.2 eV corresponding to ca. 10^{-6} atm at 400 °C), SO_4 formation on the surface is favored, which indicates the facile oxidation of SO_2 given the high O_2/SO_2 gas ratio. Further increase in SO_2 chemical potential up to ca. –1.6 eV favors the formation of adsorbed SO_3. For further increase of SO_2 chemical potential yielding a low O_2/SO_2 gas ratio, the formation of adsorbed SO_2 is most favored. Correspondingly, for a typical SO_2 chemical potential of ca. –2.2 eV in experiments, increasing the chemical potential of O_2 up to ca. –2.0 eV favors the formation of adsorbed SO_4 over the bare surface. For the same SO_2 chemical potential, further increase of O_2 chemical potential from –1.6 eV favors an O_2 covered surface. These results explain why at typical experiment conditions for methane oxidation (e.g., O_2 and SO_2 partial pressures of 0.20 atm and 10^{-6} atm, respectively), the SO_4-decorated PdO(101) surface is detected.[9,16]

Considering that the SO_4-decorated surface is highly favored at typical experiment conditions, it is imperative to describe the reaction mechanism of its formation from SO_2. Figure 6 shows the free energy profile for SO_2 oxidation to SO_4 on PdO(101) via the Eley-Rideal (red curve followed by black curve), Langmuir-Hinshelwood (black curve), and Mars-van Krevelen (blue curve) mechanisms, for temperatures of 0 K (to show the no entropic correction energy profile) and 673.15 K or 400 °C (a typical temperature in experiments where CH_4 conversion is observed.[9] The top panel in Fig. 6 shows the optimal adsorption configurations of the molecules on the surface. Briefly, in the Langmuir-Hinshelwood (LH) mechanism, both SO_2 and O_2 first adsorb onto the surface before the reaction takes place. In the Eley-Rideal (ER) mechanism, only O_2 adsorbs onto the surface; after which SO_2 interacts with the adsorbed O. Finally, in the Mars-van Krevelen (MK)mechanism, SO_2 forms a chemical bond with surface O atoms of PdO(101), generating an O vacancy site upon the production of SO_3 and SO_4.

The Gibbs free energy G_{A^*} of adsorbed species A^* ("*" denotes surface-bound species) was calculated by adding the zero point vibrational energy (ZPVE), vibrational energy change for temperature increase from 0 to T K $\left(\Delta E_{vib,0\to T}\right)$, and subtracting the vibrational entropy, as previously described in our previous works[59-60]:

$$G_{A^*} = E_{DFT} + E_{ZPVE} + \Delta E_{vib,0\to T} - S_{vib}T$$

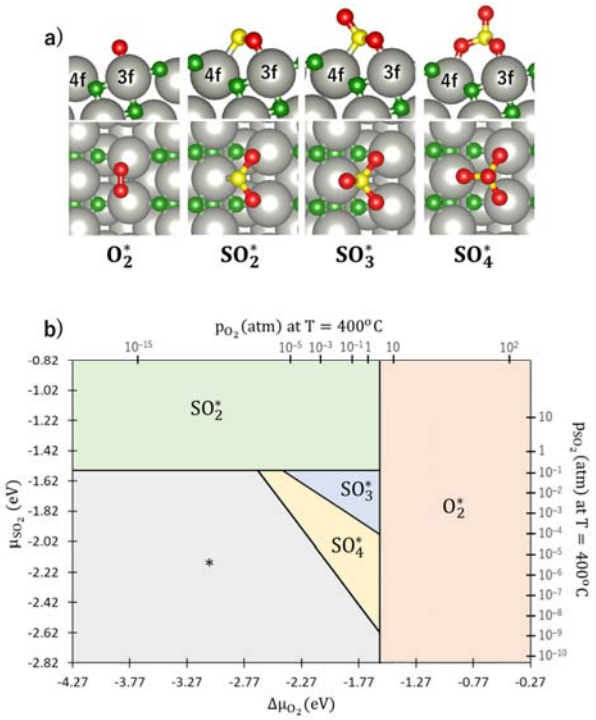

Figure 5: a) The optimal adsorption configuration of O_2, SO_2, SO_3, and SO_4 molecules without the other coadsorbed species. Red and green atoms were used to distinguish the oxygen atoms for the adsorbate and substrate respectively. The asterisk "*" denotes surface-bound species. b) Phase diagram showing the most stable adsorbed SO_y (y = 2, 3, 4) or O_2 species mapped on the chemical potentials of gas-phase SO_2 and O_2, which are translated into a pressure range for T = 400 °C. The asterisk "*" (indicating an "empty" site) shows that the clean PdO(101) surface is the most stable.

The free energies were referenced to the chemical potentials of gas-phase SO_2 and O_2, and the free energy of the slab.

It can be observed from Fig. 6 that compared to the 0 K case, the free energy profile for T = 400 °C displays higher activation energies and more endothermic reaction energies. This is due to the large increase in entropy of gas-phase O_2 and SO_2 (i.e., more negative chemical potential) which are used for reference energy. However, considering the large increase in the temperature from 0 to 400 °C, the rate constant for elementary steps are expected to increase largely, as described by the Arrhenius equation.

At this point, the energy profile for 0 K case is first described. As shown by the red curve in the ER path, the activation of O_2 requires an activation barrier of 1.68 eV (TS1). Subsequent to the dissociation of O_2, SO_2 from the gas can form a SO_3 + O coadsorption state where SO_3 binds at the Pd_{4f} atom with a planar structure. Further S–O bond formation between SO_3 and O toward the SO_4 product proceed thermodynamically downhill

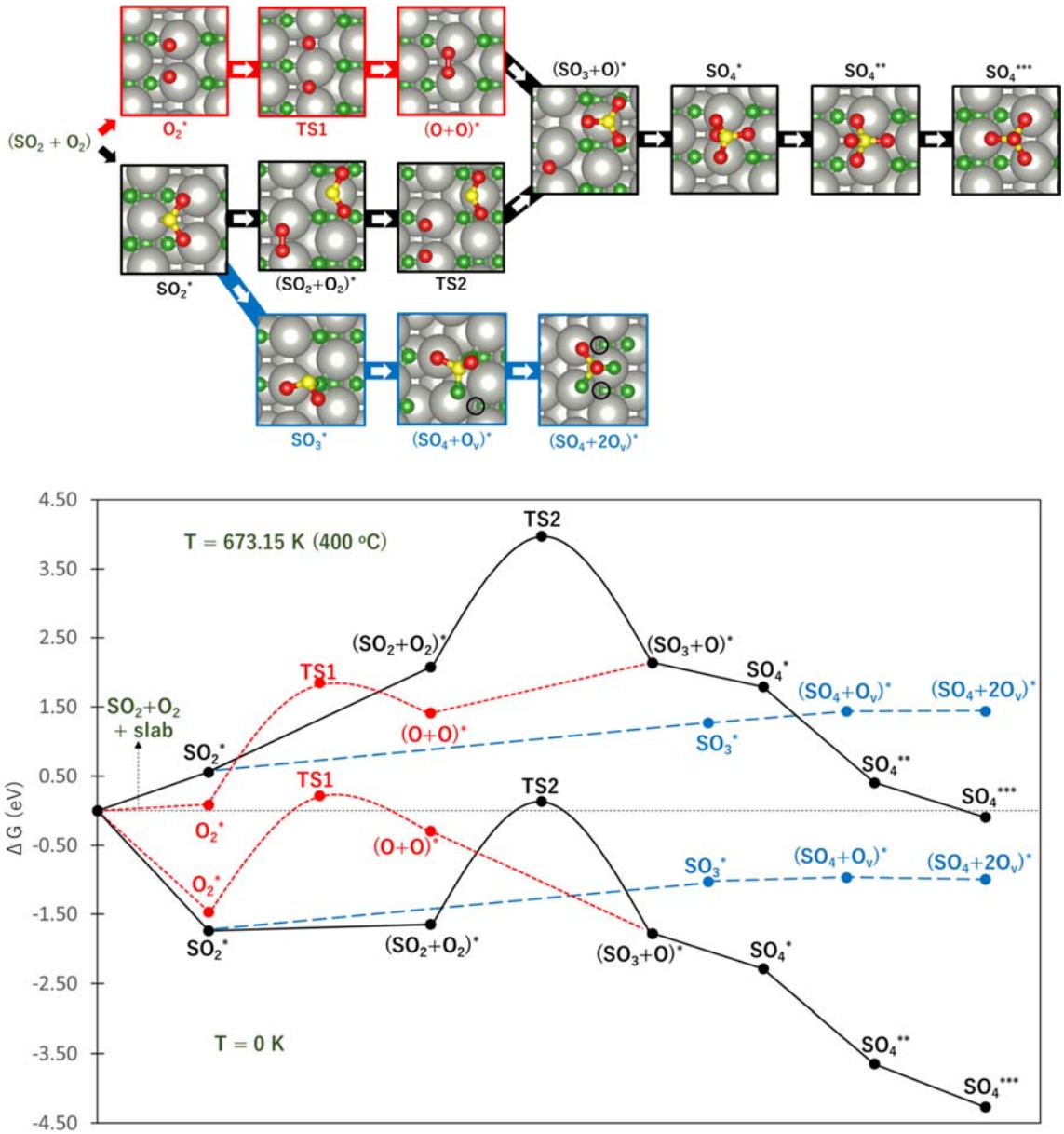

Figure 6: The upper panel shows the optimal adsorption configuration of the states depicted in the energy profile at the lower panel. The energy diagram shows the Eley-Rideal (red curve followed by black curve), Langmuir-Hinshelwood (black curve), and Mars-van Krevelen (blue curve) mechanisms, evaluated at temperatures 0 K and 673.15 K (or 400 °C).

in energy. As shown by Fig. 5, the tridentate SO_4 is most stable, followed by bidentate and monodentate structures. The reaction energy for the overall process of adsorbed SO_4 formation from the reference state is –4.27 eV.

In the LH path, SO_2 adsorbs on the surface with greater adsorption energy than molecular O_2. The coadsorption state $SO_2 + O_2$ is only slightly downhill in energy from adsorbed SO_2. This state is expected to have a lower energy in the zero coverage limit as the lateral interaction between SO_2 and O_2 becomes negligible. From the $SO_2 + O_2$ coadsorption state, the activation of O_2 requires higher energy barrier of 1.79 eV (TS2) compared to TS1, indicating a contribution from the lateral interaction between SO_2 and O + O. The subsequent S–O bond formation toward the SO_3 + O state is inferred to be barrierless as the optimization of coadsorbed SO_2 + O + O readily yields SO_3 + O.

The blue curve in Fig. 5 shows the MK path where the oxidation of SO_2 required the formation of O vacancy on the surface. The adsorbed SO_2 diffuses to a nearby O_{3f} atom to form an SO_3 species. This process is 0.71 eV endothermic. From here, the adsorbed SO_3 diffuses to the adjacent O_{3f} site forming an O vacancy and adsorbed SO_4, which is only 0.06 eV endothermic. Finally, an a slightly exothermic process proceeds, where another O vacancy is formed as SO_4 adsorbs in a tridentate structure on three coordinatively unsaturated Pd atoms. The overall process for this MK mechanism has a reaction energy of –1.00 eV with respect to the reference state.

These results show that despite the highly exothermic SO_2 oxidation on PdO(101) via the ER and LH mechanisms, its kinetics can be limited by the high barrier for O_2 dissociation. On the other hand, the MK mechanism has low exothermicity for the overall SO_2 oxidation process but is expected to promote more favorable kinetics because of relatively facile elementary steps. For the 400 ^oC case, it can be noted that the energy profile gives the same preference towards the MK mechanism. The ER and LH paths are still limited by the earlier noted activation of O_2. Similar to the 0 K case, the formation of SO_3 and SO_4 on the surface proceed downhill subsequent to the activation of O_2 for both the ER and LH mechanisms.

From these results, insights into avoiding the sulfur poisoning of PdO(101) can be drawn. Considering that CH_4 activation only involves the Pd_{3f} site while SO_2 adsorption and subsequent oxidation to SO_3 and SO_4 involve both the Pd_{3f} and Pd_{4f} sites on the PdO(101) surface, it can be argued that the Pd_{4f} site is an important element to consider in weakening/avoiding the adsorption of SO_y (x = 2 to 4) species while at the same time retaining the catalytic activity of Pd_{3f} site for methane activation. One insight is to find an adsorbate that selectively blocks the Pd_{4f} site without compromising the activity of the Pd_{3f} sites. Another approach is to replace the Pd_{4f} atoms with other elements that weakly interact with SO_y-species. These proposed approaches to catalyst design are challenged by the discovery of specific additives and impurities that would yield a sulfur poisoning resistant PdO without compromising its remarkable activity for methane oxidation. It is hoped that these insights will stimulate further research interests into the design of poison-free and efficient methane oxidation catalysts.

3. Conclusion

van der Waals-corrected density functional theory based first principles calculations were performed to determine the mechanism of PdO(101) sulfation in relation to the poisoning of the active sites for methane activation. Methane was found to adsorb at the coordinatively unsaturated Pd atom on the surface, with two C–H bonds coordinated to Pd atom and the other two C–H bonds pointing away from the surface. The unoccupied d_{zz} state of the unsaturated Pd atom facilitates the electron donation from the filled σ molecular orbital of CH_4, while its occupied d_{yz} orbital provides a back donation to the unfilled σ anti-bonding CH_4 molecular orbital, resulting in the elongation and weakening of the Pd-coordinated C–H bonds. SO_y (y = 2 to 4) species block this active site for methane activation, with the SO_4-species predicted to be most favoured at typical conditions in the experiments. The formation of SO_3 and SO_4 on the surface from the oxidation of SO_2 is highly exothermic via the Eley-Rideal and Langmuir-Hinshelwood mechanisms but is limited by the high activation barrier for O_2 dissociation. A more kinetically feasible path for SO_2 oxidation is the less exothermic Mar-van Krevelen mechanism that can provide more facile elementary steps. Results suggest that efforts in designing a sulfur poisoning resistant PdO should be aimed at blocking or substituting the four-fold coordinated Pd atom without compromising the activity of the coordinatively unsaturated three-fold Pd atom.

Computational Model

Spin-polarized DFT calculations were carried out using the Vienna ab initio simulation package (VASP).[42-45] The exchange-correlation term was described using generalized gradient approximation (GGA) based on the Perdew–Burke–Ernzerhof (PBE) functional,[48-51] with van der Waals correction (D3) by Grimme[52]. A comparison of standard GGA-DFT and GGA+U calculations for the adsorption of molecules such as H_2O, H_2, and alkanes on PdO(101) have shown similar conclusions and trends about the relative stabilities of these species on the surface.[31,57-58] Moreover, the adsorption energies and barriers of elementary processes determined through temperature program desorption (TPD) have better quantitative agreement with values calculated using the standard GGA-DFT without the +U implementation. Thus, inclusion of the +U correction to the standard GGA is expected to yield the same trend for adsorption energies of molecules and barriers for surface reactions, which is the primary interest in this paper. The interaction between ions and electrons was described using the projector augmented wave (PAW) method.[46-47] Plane wave basis sets were employed with an energy cutoff of 400 eV. The surface Brillouin zone integrations were performed on a grid of 6×6×1 Monkhorst-Pack k-points[53] using Methfessel–Paxton smearing[54] of σ = 0.2 eV.

The optimal adsorption configuration of molecules on the surface was explored using a number of different possible orientations on one side of the slab model with dipole correction to avoid spurious electrostatic interactions between

periodic images. Gas-phase molecules were modeled using one free molecule inside a 25×25×25 Å^3 unit cell. Optimizations were performed using conjugate gradient algorithm[41] to within a force tolerance of 0.05 eV/ Å. The adsorption energies of molecules were calculated by taking the difference between the total energy of the adsorbate-slab system in the lowest energy adsorption configuration and the summed energies of the optimized clean surface and the gas-phase molecule.

Acknowledgment

This work is supported in part by JST ACCEL grant number JPMJAC1501 "Creation of the Functional Materials on the Basis of the Inter-Element-Fusion Strategy and their Innovative Applications", MEXT Grant-in-Aid for Scientific Research (16K04876), and JST CREST Innovative Catalysts and Creation Technologies for the Utilization of Diverse Natural Carbon Resources: In-situ atomic characterization of catalytic reactions for the development of Innovative Catalysts (No. 17942262). Some of the numerical calculations presented here were done using the computer facilities at the following institutes: High Energy Accelerator Research Organization (KEK), Institute for Solid State Physics (ISSP, University of Tokyo), Yukawa Institute for Theoretical Physics (YITP, Kyoto University), and the National Institute for Fusion Science (NIFS). The authors acknowledge the support of Prof. Hideaki Kasai, President of the National Institute of Technology, Akashi College.

Conflicts of interest

All authors declare that they have no competing interests.

Notes and references

1) C.H. Bartholomew, *Appl. Catal. A,* 2001, 212, 17.
2) M.D. Argyle, C.H. Bartholemew, *Catalysts,* 2015, 5, 145.
3) J.P. Lange, *Angew. Chem. Int. Ed.,* 2015, 54, 13186.
4) E. Rytter, A. Holmen, *Catalysts,* 2015, 5, 478.
5) S.M. Sadrameli, *Fuel,* 2016, 173, 285.
6) I. Sadaba, M.L. Granados, A. Riisager, E. Taarning, *Green Chem.,* 2015, 17, 4133.
7) S. Ronsch, J. Schneider, S. Matthischke, M. Schluter, M. Gotz, J. Lefebvre, P. Prabhakaran, S. Bajohr, *Fuel,* 2016, 166, 276.
8) R.L. Arevalo, S.M. Aspera, M.C.S. Escano, H. Nakanishi, H. Kasai, *Sci. Rep.*, 2017, 7, 13963.
9) P. Gelin, M. Primet, *Appl. Catal. B,* 2002, 39, 1.
10) H.N. Sharma, V. Sharma, A.B. Mhadeshwar, R. Ramprasad, *J. Phys. Chem. Lett.*, 2015, 6, 1140.
11) A. Gremminger, P. Lott, M. Merts, M. Casapu, J.-D. Grunwaldt, O. Deutschmann, *Appl. Catal. B,* 2017, 218, 833.
12) S. Colussi, F. Arosio, T. Montanari, G. Busca, G. Groppi, A. Trovarelli, *Catal. Today,* 2010, 155, 59.
13) S. Ordonez, P. Hurtado, F.V. Diez, *Catal. Lett.*, 2005, 100, 27.
14) M. Happel, Y. Lykhach, N. Tsud, T. Skala, V. Johanek, K.C. Prince, V. Matolin, J. Libuda, *J. Phys. Chem. C,* 2012, 116, 10959.
15) D. Mowery, R.L. McCormick, *Appl. Catal. B,* 2001, 34, 287.
16) J.K. Lampert, M. Shahjahan Kazi, R.J. Farrauto, . *Appl. Catal. B,* 1997, 14, 211.
17) L.J. Hoyos, H. Praliaud, M. Primet, . *Appl. Catal. A,* 1993, 98, 125.
18) M.S. Wilburn, W.S. Epling, *Appl. Catal. B,* 2017, 206, 589.
19) V. Meeyoo, D.L. Trimm, . *Appl. Catal. B,* 1998, 16, L101.
20) P. Briot, M. Primet, *Appl. Catal.,* 1991, 68, 301.
21) J.M. Jones, V.A. Dupont, R. Brydson, D.J. Fullerton, N.S. Nasri, A.B. Ross, A.V.K. Westwood, *Catal. Today,* 2003, 81, 589.
22) D. Ciuparu, M.R. Lyubovsky, E. Altman, L.D. Pfefferle, A. Datye, *Catal. Rev.*, 2002, 44, 593.
23) S.K. Matam, M.H. Aguirre, A. Weidenkaff, D. Ferri, *J. Phys. Chem. C,* 2010, 114, 9439.
24) R. Westerstrom, M.E. Messing, S. Blomberg, A. Hellman, H. Gronbeck, J. Gustafson, N.M. Martin, O. Balmes, R. van Rijn, J.N. Andersen, K. Deppert, H. Bluhm, Z. Liu, E. Grass, M. Havecker, E. Lundgren, *Phys. Rev. B,* 2011, 83, 115440.
25) R. van Rijn, O. Balmes, A. Resta, D. Wermeille, R. Westerstrom, J. Gustafson, R. Felici, E. Lundgren, J.W.M. Frenken, *Phys. Chem. Chem. Phys.*, 2011, 13, 13167.
26) A. Hellman, A. Resta, N.M. Martin, J. Gustafson, A. Trinchero, P.-A. Carlsson, O. Balmes, R. Felici, R. van Rijn, J.W.M. Frenkeni, J.N. Andersen, E. Lundgren, H. Gronbeck, *J. Phys. Chem. Lett.,* 2012, 3, 678.
27) J.F. Weaver, C. Hakanogly, A. Antony, A. Asthagiri, *Chem. Soc. Rev.*, 2014, 43, 7536.
28) J.G. McCarty, *Catal. Today,* 1995, 26, 283.
29) C.-J. Huang, F.-M. Pan, T.-C. Tzeng, L. Chang, J.-T. Sheu, *J. Elec. Soc.*, 2009, 156, J28.
30) H.H. Kan, J.F. Weaver, *Surf. Sci.*, 2008, 602, L53.
31) J.F. Weaver, C. Hakanoglu, J.M. Hawkins, A. Asthagiri, *J. Chem. Phys.,* 2010, 132, 024709.
32) M. Van den Bossche, H. Gronbeck, *J. Am. Chem. Soc.*, 2015, 137, 12035.
33) P. Xiao, D. Sheppard, J. Rogal, G. Henkelman, *J. Chem. Phys.*, 2014, 140, 174104.
34) J. Kastner, P. Sherwood, *J. Chem. Phys.*, 2008, 128, 014106.
35) A. Heyden, A.T. Bell, F.J. Keil, *J. Chem. Phys.*, 2005, 123, 224101.
36) G. Henkelman, H. Jonsson, *J. Chem. Phys.*, 1999, 111, 7010.
37) J.F. Weaver, J.A. Hinojosa, C. Hakanogly, A. Antony, J.M. Hawkins, A. Asthagiri, *Catal. Today,* 2011, 160, 213.
38) Y.-H. Chin, C. Buda, M. Neurock, E. Iglesia, *J. Am. Chem. Soc.,* 2013, 135, 15425.
39) C.-C. Wang, S.S. Siao, J.-C. Jiang, *J. Phys. Chem. C,* 2012, 116, 6367.
40) J. Au-Yeng, K. Chen, A.T. Bell, E. Iglesia, *J. Catal.*, 1999, 188, 132.
41) I. Stich, R. Car, M. Parrinello, S. Baroni, *Phys. Rev. B,* 1989, 39, 4997.
42) G. Kresse, J. Furthmuller, *Phys. Rev. B,* 1996, 54, 11169.
43) G. Kresse, J. Furthmuller, *Comput. Mater. Sci.*, 1996, 6, 15.
44) G. Kresse, J. Hafner, *Phys. Rev. B,* 1993, 47, 558.
45) G. Kresse, J. Hafner, *Phys. Rev. B,* 1994, 49, 14251.
46) P. Blochl, *Phys. Rev. B,* 1999, 59, 17953.
47) G. Kresse, J. Joubert, *Phys. Rev. B,* 1999, 59, 1758.
48) J. Perdew, K. Burke, M. Ernzerhof, *Phys. Rev. Lett.*, 1996, 77, 3865.
49) J. Perdew, K. Burke, *Phys. Rev. B,* 1996, 54, 16533.
50) A. Becke, *Phys. Rev. A,* 1988, 38, 3098.
51) C. Lee, W. Yang, R. Parr, *Phys. Rev. B,* 1988, 37, 785.
52) S. Grimme, *J. Comp. Chem.*, 2004, 25, 1463.
53) H. Monkhorst, *Phys. Rev. B,* 1976, 13, 5188.
54) M. Methfessel, A. Paxton, *Phys. Rev. B,* 1989, 470, 3616.
55) M.J. Frisch, et al., Gaussian 09, Gaussian, Inc., Wallingford CT, 2009.
56) K. Momma, F. Izumi, *J. Appl. Cryst.*, 2011, 44, 1272.
57) C. Hakanoglu, J.M. Hawkins, A. Asthagiri, J.F. Weaver, *J. Phys. Chem. C*, 2010, 114, 11485.
58) H.H. Kan, R.C. Colmyer, A. Asthagiri, J.F. Weaver, *J. Phys. Chem. C*, 2009, 113, 1495.
59) R.L. Arevalo, M.C.S. Escano, H. Kasai, ACS Catal., 2013, 3, 3031.
60) R.L. Arevalo, M.C.S. Escano, A.Y.-S. Wang, H. Kasai, Dalton Trans., 2013, 42, 770.